SIMULATION OF TURBULENT FLOW BETWEEN TWO SQUARE CYLINDERS IN TANDEM ARRANGEMENT WITH DIFFERENT TURBULENCE MODELS

D. Hartmann
Faculty of Mechanical Engineering, RWTH Aachen
Templergraben 55, 52056 Aachen

1. INTRODUCTION

The flow field around bluff bodies, such as cylinders, is frequently observed to be unsteady, and characterized by massive separation. A phenomenon initiated by this separation is vortex shedding, which occurs in the wake of bluff bodies.

Thorough analyses of the flow field around two-cylinder set-ups started rather late in comparison with investigations into single cylinder set-ups [13]. This was due to the assumption that interference effects between the two cylinders were negligible. However, this assumption proved to be wrong, because the flow field around the cylinders in a twin set-up may differ greatly from the one around a single cylinder. The upstream cylinder faces the free stream with a relatively low turbulence level, whereas the downstream cylinder is exposed to the wake of the upstream cylinder, which causes a turbulent flow field and often oscillating velocity fluctuations.

Extensive investigations have been undertaken for circular cylinders in single and tandem arrangement, while square cylinders were mainly addressed for a single set-up. Sakamoto et al. [11] provide a comprehensive set of data in terms of the Strouhal number, which characterizes the vortex shedding frequency, and force coefficients for a wide range of two square cylinder set-ups in tandem arrangement. However, analyses of turbulence quantities are presently not available for this flow case. Also, numerical computations have mainly focused on the flow case around single bluff bodies, such as in [2].

In the present work, the flow field around a pair of square cylinders in tandem configuration is investigated numerically and compared to experimental results obtained from Particle Image Velocimetry (PIV) measurements. Changes of the flow regime due to a different distance of the two cylinders are taken into account and examined. Furthermore, steady and unsteady computations are carried out on the basis of the Reynolds averaged Navier-Stokes (RANS) equations. A number of variations of the $k-\varepsilon$ model is employed, and the results are compared with the experiment.

2. MATHEMATICAL MODEL

The Reynolds-averaged Navier-Stokes equations read

$$(1)\quad \frac{\partial U_i}{\partial t}+U_j\frac{\partial U_i}{\partial x_j}=-\frac{1}{\rho}\frac{\partial P}{\partial x_i}+\upsilon\nabla^2 U_i-\frac{\partial \overline{u_j u_i}}{\partial x_j},\qquad \frac{\partial U_i}{\partial x_i}=0$$

where j is a running index, x_α is the coordinate in space direction α, and U_α and P denote averaged velocity and pressure, respectively. $\overline{u_j u_i}$ is the Reynolds stress tensor, which is unknown. In the standard $k-\varepsilon$ model, this term is connected to the eddy viscosity υ_T through

$$(2)\quad -\overline{u_j u_i}=2\upsilon_T S_{ij}-\frac{2}{3}k\delta_{ij},$$

where δ_{ij} is the Kronecker δ and $S_{ij}=\left(\frac{\partial U_i}{\partial x_j}+\frac{\partial U_j}{\partial x_i}\right)$.

Using further approximations, υ_T can be traced back to the turbulent kinetic energy k and the rate of dissipation of turbulent kinetic energy ε:

$$(3)\quad \upsilon_T=C_\mu\frac{k^2}{\varepsilon},$$

with the standard value for $C_\mu=0.09$.

The equations for k and ε as well as the formulation of υ_T, which is given by Equ. (3) for the standard model, depend on the type of $k-\varepsilon$ model which is used. Details can be found in [5].

2.1. Boundary Conditions

The computational domain is given by FIG. 1. The inflow plane is located at $x/H=-11$ (a distance of $10H$ away from the upstream cylinder), while the outflow boundary is located at a distance of $20H$ behind the downstream cylinder. These values are chosen according to [2], such that the presence of the boundaries does not influence the flow field in concern. The width of the computational domain is $B=10H$ in accordance with the PIV experiments that were carried out as reference. This gives a blockage of $H/B=10\%$.

The inflow boundary condition for the free stream velocity u_∞ is also chosen in accordance with the PIV experiments, see Equ. (6). Turbulent kinetic energy k and turbulent dissipation rate ε at the inflow are estimated using the Equations [5]

$$(4)\quad k=\frac{3}{2}(u_\infty I)^2$$

and

$$(5)\quad \varepsilon=C_\mu^{3/4}\frac{k^{3/2}}{l},\quad C_\mu=0.09.$$

The turbulence intensity was found to be $I=1\%$ in the experiment and the turbulent length scale is estimated as $l=0.07H$. Thus, the inflow conditions read

$$(6)\quad u_\infty=0.3\ \text{m/s}$$

$$(7)\quad k=1.35\cdot10^{-5}\ \text{m}^2/\text{s}^2$$

(8) $\varepsilon = 3.88 \cdot 10^{-6}$ m²/s³.

All outflow conditions are treated by FLUENT. They include a zero diffusion flux condition for all variables and an overall mass balance condition [5]. A symmetry condition is applied to the upper and lower boundaries of the computational domain.

2.2. Wall Treatment

The greatest disadvantage of the $k-\varepsilon$ model is its failure to correctly model the near-wall characteristics of turbulent flows. Particularly, it overestimates the turbulent mixing in the flow near walls, which is actually suppressed in these areas. Hence, a wrong profile of the eddy viscosity is calculated.

Two commonly used approaches to improve the near-wall behavior of the $k-\varepsilon$ model are the introduction of wall functions and the modification of the model itself. While the former are of semi-empirical nature and assume a flow field behavior according to a prescribed function, the latter enable to resolve the near-wall region all the way to the wall. However, this requires an appropriately fine mesh in this region and thus considerably increases computational effort.

In the present thesis, a two-layer approach is used in order to bridge the viscous near-wall region. The computational domain is subdivided into a viscosity-affected region and a fully-turbulent region [5]. In the fully-turbulent high-Reynolds-number region, the $k-\varepsilon$ model is employed, while the one-equation model of Wolfstein is used for the viscosity-affected region. In order to ensure a smooth transition between the two regions, the corresponding definitions of the turbulent viscosity as well as the specification of ε are blended. Details can be found in [5].

2.3. Method of Solution

For the computations, FLUENT 6.1 is used on LINUX machines featuring a Pentium 4 3.06 GHz CPU and 1 GB of main memory.

The solution is obtained in two steps. First, a conservative calculation using standard wall functions as well as a low order discretization scheme is undertaken, being followed by a second iteration approach using the two-layer approach near walls. Furthermore, a second-order upwind discretization scheme is then used for the k and ε transport equations as well as a second order approach is used for the pressure interpolation. The pressure-velocity coupling is handled with the PISO algorithm, while the QUICK (Quadratic Upwind Interpolation for Convective Kinematics) scheme is employed only for the momentum equation. Although it may offer a higher accuracy, it is not used for discretization of the transport equations. For these, it was found to be not suitable [2].

3. STEADY CALCULATIONS

In the following, results of steady RANS computations using various $k-\varepsilon$ models are given and compared to ensemble-averaged experimental data obtained from PIV measurements. Two flow cases are investigated, namely $D/H=3$, and $D/H=2$. As a result of grid convergence tests, the grid shown in FIG. 2(a) is used for steady computations ($D/H=3$). The number of grid lines at the outer boundaries is 248×69 for the case $D/H=3$ and 217×69 for the case $D/H=2$ respectively. In addition, the grid is adapted near the cylinder walls during the calculation in order to assure $y^+ \approx 1$ in these areas. The adaptation includes refinement as well as coarsening and is automatically accomplished by FLUENT. The number of added cells due to this adaptation is found to be smaller than 100 and depends on the state of the solution at which the adaptation is performed. The convergence criterion is 10^{-5} for the scaled residuals of pressure, pressure-velocity-coupling, momentum and transport equations.

3.1. Case *D/H*=3

In this section, the case $D/H=3$ is investigated. For this setup, vortex shedding is observed in PIV experiments [6]. Comparing the streamlines, FIG. 3, one recognizes a great difference between the results of the steady RANS computations and the experiment.

The recirculation regions being predicted by all three computations extend over the entire region between the two cylinders, whereas the experimental results show a closed recirculation region. Comparing the different RANS models, the recirculation region calculated by the RNG $k-\varepsilon$ and realizable $k-\varepsilon$ model is larger in terms of its extension in y direction than the one calculated by the standard $k-\varepsilon$ model.

FIG. 4 shows contours of the stream function

(9) $$\psi = \int_0^y \hat{u} \cdot dy$$

As from the above definition is clear, the integration is started at the center line, which coincides with the symmetry line. Hence, $\psi = 0$ along $y = 0$. The observations made above are clarified by FIG. 4, while the length of the recirculation region given by the experiment can be determined to be $x = 0.94$, FIG. 4(a).

FIG. 5 illustrates further details of the recirculation regions predicted by the different $k-\varepsilon$ models. FIG. 5(b)-(d) depict that both the RNG $k-\varepsilon$ and realizable $k-\varepsilon$ model predict a more consolidated recirculation region than the standard model does. Following that the recirculation regions are extended beyond the height of the cylinders, FIG. 5(b)-(d), there is also no separation at the windward face of the downstream cylinder in the computed flow field. However, this can be assumed to be the case for the ensemble-averaged flow field obtained from the experiment, FIG. 5(a).

3.2. Case *D/H*=2

Experiments show that an oscillatory flow field motion at a constant (dominant) frequency cannot be found for the case $D/H=2$ [6]. Since no vortex shedding occurs behind the upstream cylinder, the steady RANS calculations represent the experimental results better than in the case $D/H=3$, for which vortex shedding is observed.

The streamline plots, FIG. 6, show a large recirculation region in the experimental result, which is also acquired by the computations. However, the calculated extension of this region deviates significantly from the experimental result. FIG. 7 clarifies, that the experimental result yields a recirculation zone which is stretched to about $y/H=1$, while the computations show a more consolidated recirculation region which extends to about $y/H=0.75$. Also, the experiment shows larger velocity gradients along the boundaries of the recirculation region than the computations do, as it can be deduced from the dramatic change of

distance between streamlines (lines of constant ψ) of succeeding values in this area. Here, an accumulation of streamlines in the detached shear layer region is adjacent to the recirculation region with very low velocities, FIG. 7(a) and 8(a). The RANS computations give a lower density of lines in this region, FIG. 7(b)-(d), and thus a less dramatic change of velocity with respect to the recirculation region.
The contour plots of the velocity magnitude and the corresponding velocity vectors, FIG. 8, also depict the more stretched recirculation region of the experimental results and therefore show some differences in the distribution of velocity magnitude. Furthermore, they emphasize the similarity of the results obtained by the three different $k-\varepsilon$ models.
In summary, it can be said that steady RANS computations with the examined $k-\varepsilon$ models do not give satisfactory results for the case $D/H=3$, which involves vortex shedding behind the upstream cylinder. The predicted recirculation regions are by far too large, although the results of the RNG $k-\varepsilon$ and realizable $k-\varepsilon$ model appear to be slightly superior to the result delivered by the standard $k-\varepsilon$ model. For the case $D/H=2$, for which vortex shedding behind the upstream cylinder is not observed, a better agreement of experimental and computational results is obtained. The predicted recirculation regions deviate from the experimental results, but within a reasonable accuracy.

4. UNSTEADY CALCULATIONS

Other than in the previous section, where the flow case is changed in order to reach a steady state, the approach being described in this section is based on the entire flow field and uses time-dependent calculations. In this section, the computational results obtained from unsteady RANS (URANS) calculations are presented.
In URANS computations, the time domain is split up into time steps of a prescribed length. For each of these time steps, a solution is calculated to 10^{-5} convergence of the scaled residuals. An initial time step $\Delta t^* = 0.02$ is chosen and a second-order implicit unsteady formulation is used. This non-dimensional time step $\Delta t^* = H/u$ is proposed by Bosch and Rodi [2] and is found to be appropriate for some cases. However, it is decreased when the solution does not converge within 50 iterations for each time step. According to the half size grid used for steady calculations, the number of grid lines of the full mesh at the outer boundaries is 248×138 for the case $D/H=3$ and 217×138 for the case $D/H=2$, respectively. In terms of the condition $y^+\approx1$ at the cylinder walls, an automatic grid adaptation by FLUENT is performed after several time steps. However, as the flow field changes with time, so do the values of y^+ at the cylinder walls. Therefore, one has to be content with y^+ being approximately on the order of 1.
While a pressure fluctuation was measured in the PIV experiments in order to determine oscillatory motion of the flow field, the fluctuation of drag coefficients is monitored for both the upstream and downstream cylinder in the numerical computations. Moreover, these coefficients are used to determine convergence of the unsteady solution, which should not be mistaken for the above mentioned convergence of scaled residuals. In order to exemplify this procedure, the drag coefficient data obtained by the standard $k-\varepsilon$ model for the case $D/H=3$, for which a time step $\Delta t^* = 0.02$ is used, is given in FIG. 9.
FIG. 9 shows, that the drag coefficients vary over a wide range of values in the initial stage of the unsteady computation. After about two seconds of solution time, i.e., 1000 time steps, a regular periodic change of c_d values emerges. Thereby, the c_d peak values converge to a limiting value. Further investigations of convergence are undertaken for the drag coefficient of the upstream cylinder, FIG. 10, since a similar rate of convergence is expected for the values of the downstream cylinder. Since the convergence is not monotonic, as FIG. 10(b) depicts, Richardson extrapolation cannot be used for error estimates. Therefore, the relative change of succeeding c_d peak values is observed, FIG. 10(b), and a convergence criterion for c_d is prescribed to be 10^{-4}.
The abovementioned periodic change of c_d suggests an oscillatory motion of the flow field, as it is found in the case of the PIV experiment for $D/H=3$. In the experiment however, the pressure fluctuation is monitored only at one specific location [6]. By contrast, drag coefficients are addressed to the entire upstream or downstream cylinder. This has a great effect on the conclusions that can be drawn.
Whereas for the analysis of experimental data, one periodic pressure cycle is recognized to be equivalent to one periodic cycle of flow field motion, one cycle of the monitored drag coefficient of a cylinder is addressed to only half a cycle of flow field motion. This is due to the fact that the flow patterns which are released from the upper and lower side of the upstream cylinder are symmetric about the center line at $y=0$ and occur with a time shift of half a periodic cycle. Hereby, both patterns have a frequency according to the periodic cycle length of the whole flow field motion. If one measures the static pressure on one side of the cylinder, as in the case of the experiment, one will receive a periodic change of this quantity according to the respective flow field on this side, i.e., the frequency of this change resembles the frequency of the whole flow field motion.
However, measuring the drag coefficient of the cylinder, both flow patterns are involved. Since they are temporally shifted by half a cycle length and have an equal effect on c_d, the measured drag coefficient will periodically change with twice the frequency of the whole flow field motion. Recapitulating, in order to receive an ensemble-averaged flow field, the samples of two periodic cycles that are monitored for the drag coefficient have to be averaged.
FIG. 11 illustrates the length of c_d cycles between two succeeding peaks. It is shown that the cycle lengths vary with time and do not appear to be converging to a limiting value. The dashed line represents the average cycle length of all displayed cycles. For evaluation, two cycles with a similar cycle length near the average value are selected.
The above described procedure is adopted to each of the time-dependent computations, if a periodic c_d value pattern is observed. In the following subsections, the results of these URANS computations are presented.

4.1. Case *D/H*=3

In this section, the results of URANS calculations using the standard, RNG $k-\varepsilon$ and realizable $k-\varepsilon$ model are compared to the experimental results for the flow case $D/H=3$. FIG. 12 shows the streamline plots of the entire investigated flow field between the two cylinders. Clearly, the streamline plots obtained from the RNG $k-\varepsilon$ and realizable $k-\varepsilon$ model, FIG. 12(c)-(d), represent the experimental data, FIG. 12(a), fairly well. Essentially, no difference can be seen between the plots from them.

By contrast, the standard $k-\varepsilon$ model gives a too large recirculation region, which appears to be only slightly smaller than the one calculated by the steady RANS models. This is supported by the contour plots of the stream function, Equ. (1). FIG. 13 clearly points out the similarity of the results from the RNG and realizable model and their rather good accordance to the experimental result compared to the standard $k-\varepsilon$ model, which is again seen to predict a recirculation region extending over the entire distance between the two cylinders. Interestingly, the recirculation regions calculated by the RNG and realizable model appear to be smaller than the one obtained from the experiment. The calculated lengths of the recirculation regions at $y=0$ are $x/H=0.87$ (RNG model) and $x/H=0.84$ (realizable model), compared to $x/H=0.94$ which is obtained from the experiment. The corresponding errors come to 7.4% for the RNG model and 10.6% for the realizable model, respectively. Furthermore, the stream function plot of the experimental data, FIG. 13(a), indicates larger velocity gradients along the boundaries of the recirculation area compared to the results obtained by the RNG and realizable $k-\varepsilon$ model. This can again be followed from the density of streamlines in the respective area. For $0\le y/H\le 0.5$, FIG. 14 illustrates a large difference in velocity magnitude downstream of $x/H=1$ between the results of the experiment and the RNG $k-\varepsilon$ and realizable $k-\varepsilon$ model. The computations give a three times larger value than the experiment.

All three models show an oscillating drag coefficient. However, the Strouhal number, which is deduced from the c_d oscillations, deviates from the experimental result, as Table 1 shows. It is underestimated by 6% by the standard model and overestimated by more than 10% by the RNG and realizable model.

Furthermore, Table 1 compares the calculated drag coefficients with results found by Sakamoto et al. [11]. All employed models deviate from Sakamoto's results. While the drag coefficient of the upstream cylinder is underestimated by all three $k-\varepsilon$ models but is somewhat near the reference value (with errors ranging from 20% for the RNG and the realizable model to 30% for the standard model), the calculated values for the downstream cylinder are far apart from the reference value. The standard $k-\varepsilon$ model underestimates the drag coefficient of the downstream cylinder by more than a third, while the RNG $k-\varepsilon$ and realizable $k-\varepsilon$ model calculate a value which is more than three times too large and more than two times too large, respectively.

The very poor agreement in terms of the drag coefficient of the downstream cylinder points to the fact, that the seemingly good accordance of the recirculation regions which were given by the experiment and calculated by the RNG $k-\varepsilon$ and realizable $k-\varepsilon$ model does not prevent very large differences in the region around the downstream cylinder, as it was stated above in terms of the velocity magnitude.

Finally, streamline plots at different solution times are shown in order to compare the unsteady flow field patterns that the $k-\varepsilon$ models give, FIG. 15. The quantity t_s is introduced in order to denote the length of one shedding cycle for each model. Reference quantity for the oscillating flow field motion is the drag coefficient of the upstream cylinder. Hereby, the beginning and end of such a cycle are marked by peaks of this drag coefficient. The flow patterns of the RNG and realizable model almost coincide. The wavy pattern of the wake flow and the strong vortex shedding is quite similar to that observed in the experiment [6]. By comparison, the standard $k-\varepsilon$ model calculates rather large vortices that travel downstream between the two cylinders and, by contrast to the experimental results, do not cross the center line at $y=0$. However, this behavior is captured by both the RNG and realizable model. In the solution of the standard model, a closed vortex structure can be found to travel all the way to the downstream cylinder, which is in contrast to the experimental result [6], and the results reported for the RNG and realizable model. Thus, stronger vortex structures, whose shedding by the upstream cylinder appears weaker, can be monitored for the standard model. This is in accordance with the results reported by Bosch and Rodi [2] for the one-cylinder case.

The result of the standard model furthermore shows that the streamlines above the separated shear layers on the upper side of the cylinder, and below the separated shear layers on the lower side of the cylinder respectively, do not intrude the wake flow at any of the given instants. This is in contrast to the experimental result, where these streamlines go across the entire flow field [6]. This is also predicted by the RNG and realizable $k-\varepsilon$ model, e.g. FIG. 15(e).

FIG. 16 shows the distribution of ensemble-averaged turbulent kinetic energy k and brings forward a known deficiency of the standard $k-\varepsilon$ model. In front of the upstream cylinder, an increase of turbulent kinetic energy is obtained by the standard $k-\varepsilon$ model, which is not observed in the solutions of the RNG $k-\varepsilon$ and realizable $k-\varepsilon$ model. According to Bosch and Rodi [2], this increase is significant for the flow behavior in the wake region. Furthermore, FIG. 16 shows that, in comparison with the RNG and realizable model, the standard model gives an excessive distribution of turbulent kinetic energy in the separated shear layer regions, which is propagated downstream all the way to the downstream cylinder. With regards to FIG. 15, the increased k is recognized to cause a weaker vortex shedding in the solution of the standard $k-\varepsilon$ model. This is understood such that energy of the mean flow is dumped out in regions of large k, which consequently reduces oscillatory flow field motion.

FIG. 17 depicts the distribution of eddy viscosity for the three models at the solution times corresponding to FIG. 15(a), (d) and (g). With regards to Equ. (4.6), an increase of k increases υ_T as well. With reference to FIG. 15(d) and (g), a region of large υ_T extends around $(x/H, y/H)=(1.5,-1)$ below the closed vortex in the solutions of the RNG $k-\varepsilon$ and realizable $k-\varepsilon$ model. Al-

though the streamline plots shown by FIG. 15 do not indicate greater differences between the solutions of the RNG $k-\varepsilon$ and the realizable $k-\varepsilon$ model, the calculated υ_T diverges around $(x/H, y/H) = (1.5, -1)$. The realizable model gives a steep peak, with a value being twice as large as the rather constant values obtained by the RNG model in this area.
However, FIG. 17 indicates a predominance of small υ_T, allowing the distinctive oscillatory flow field motion, which is captured by the RNG and realizable model. The connection between υ_T and mean flow energy can be recognized from the similar wavy patterns of the distribution of small υ_T on the one hand and streamlines on the other hand.
By contrast to the RNG and realizable model, the standard $k-\varepsilon$ model gives comparatively large values of υ_T in the entire area of concern, resulting in a weaker oscillatory motion of the flow field, FIG. 17(a). A reason for these large values can be found in the extended region of increased υ_T in front of the upstream cylinder, which stems from a similar distribution of k in this area, FIG. 16.

4.2. Case *D/H=2*

In this section, unsteady $k-\varepsilon$ model calculations for the flow case $D/H = 2$ are compared against the experimental data. The solution process already shows a difference between the standard model and the RNG and realizable model. The former model yields steady values for the drag coefficients and thus, a steady solution. By contrast, the RNG and realizable model calculate oscillating drag coefficients and in fact periodic vortex shedding behind the upstream cylinder. FIG. 18 shows the streamlines obtained from the RNG $k-\varepsilon$ model. The corresponding plots obtained by the realizable model are omitted since they appear alike.
The results of the time-dependent computation resemble the findings of the steady calculation, FIG. 6-8, to a large extent. The corresponding figures are therefore omitted. FIG. 19 shows the distribution of ensemble-averaged turbulent kinetic energy in the surroundings of the upstream cylinder. Same as for the previous case $D/H = 3$, the increased turbulent kinetic energy in the result of the standard model is emphasized. However, it is not connected to the wake flow of the upstream cylinder. Since vortex shedding behind the upstream cylinder is not observed for the present flow case, the result of the standard model for the region in concern between the cylinders is understood not to be greatly affected by the increased turbulent kinetic energy in the shear layer regions.
TAB. 2 compares the calculated drag coefficients of the upstream and downstream cylinder. By contrast to the case $D/H = 3$, the values agree much better with the given reference values by Sakamoto et al. [11]. The calculated drag coefficients for the upstream cylinder differ by 8.6% for the standard $k-\varepsilon$ model, 4.6% for the RNG $k-\varepsilon$ model and 3.4% for the realizable $k-\varepsilon$ model. Against the background of the expected discretization error, which is of about the same order of magnitude as these differences, this is a satisfactory result for all models. However, in spite of the good agreement in terms of the upstream cylinder, the drag coefficient of the downstream cylinder is underestimated. The RNG and the realizable model yield a difference of 50% and 35%, respectively, while the standard model underestimates the reference value by more than a third.

5. SUMMARY

In the present work, the flow field around two square cylinders was investigated. In particular, the wake region of the upstream cylinder, i.e., the area between the two obstacles was examined.
A computational approach was undertaken in order to clarify the scope of application of three kinds of $k-\varepsilon$ models for the investigated flow cases. Both steady and unsteady RANS computations were carried out for the flow cases $D/H = 3$ and $D/H = 2$.
For $D/H = 3$, the standard $k-\varepsilon$ model did not deliver reasonably accurate results for both the steady and unsteady RANS approach. The predicted vortex shedding was too weak, which agrees with published results for a single square cylinder. Also the RNG $k-\varepsilon$ and realizable $k-\varepsilon$ model were not capable of accurately predicting the flow field in steady computations. However, the unsteady RANS approach using these models delivered satisfactory results in the vicinity of the upstream cylinder, which dramatically degraded near the downstream cylinder. These results were especially reflected by the calculated drag coefficients of the downstream cylinder, which showed large deviations from published reference values.
For $D/H = 2$, the two large recirculation zones that were obtained from the experimental results were captured by all investigated models. Thereby, the unsteady RANS computations did not deliver better results than the steady RANS computations. Similar to the case $D/H = 3$, comparison of the drag coefficients yielded satisfactory agreement only for the upstream cylinder. The computational solutions in the vicinity of the downstream cylinder degraded.

6. ACKNOWLEDGEMENTS

This work was carried out as part of the author's thesis [6] at the Department of Mechanical Engineering, Keio University, and was supported by the German Academic Exchange Service (DAAD). The author would like to thank Prof. S. Obi and his students for their invaluable guidance and support.

REFERENCES

[1] Bernard, P.S.; Wallace, J.M.: „Turbulent flow." John Wiley & Sons, Inc., Hoboken, New Jersey, 2002.
[2] Bosch G.; Rodi, W.: „Simulation of vortex shedding past a square cylinder with different turbulence models." International Journal for Numerical Methods in Fluids, vol. 28, pp. 601-616, 1998.
[3] Durbin, P.A.; Petterson Reif, B.A.: „Statistical theory and modeling for turbulent flows." John Wiley & Sons, Ltd., Chichester, 2001.
[4] Ferziger, J.H.; Peric, M.: „Computational methods for fluid dynamics." Springer-Verlag, Berlin, Heidelberg, 1999.
[5] „FLUENT 6.1, User's Guide." Fluent Inc., 2003.
[6] Hartmann, D.: "Experimental study on turbulent flow around two bluff bodies in uniform flow in tandem." Student thesis, RWTH Aachen and Keio University, 2004.
[7] Kolář, V; Lyn, D.A.; Rodi, W.: „Ensemble-averaged measurements in the turbulent near wake of two side-

by-side square cylinders." Journal of Fluid Mechanics, vol. 346, pp. 201-237, 1997.

[8] Lyn, D.A.; Rodi, W.: „The flapping shear layer formed by flow separation from the forward corner of a square cylinder." Journal of Fluid Mechanics, vol. 267, pp. 353-376, 1994.

[9] Lyn, D.A.; Einav, S.; Rodi, W.; Park, J.-H.: „A laser-Doppler velocimetry study of ensemble-averaged characteristics of the turbulent near wake of a square cylinder." Journal of Fluid Mechanics, vol. 304, pp. 258-319, 1995.

[10] Obi, S.; Tokai, N.; Sakai, K.: „The role of pressure-velocity correlation in oscillatory flow between a pair of bluff bodies." To be presented at the ERCOFTAC International Symposium on Engineering Turbulence Modelling and Measurements, Sardinia, 2005.

[11] Sakamoto, H; Haniu, H.; Obata, Y.: „Fluctuating forces acting on two rectangular prisms in tandem arrangements." Transactions of the Japan Society of Mechanical Engineering, **52**-484, B(1986), 3964.

[12] Tennekes, H.; Lumley, J.L.: A first course in turbulence." The MIT Press, Cambridge, 1972.

[13] Zdravkovich, M.M.: „Flow around circular cylinders, Vol. 2 Applications." Oxford University Press Inc., New York, 2003.

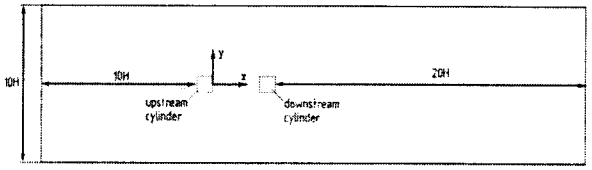

FIG. 1. Computational domain

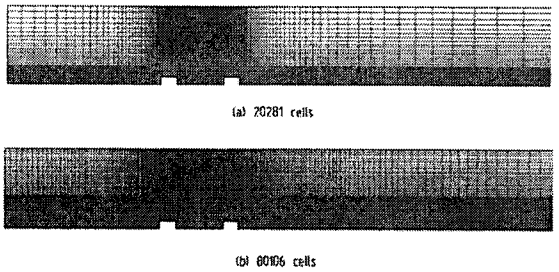

FIG. 2. Comparison of two selected grids

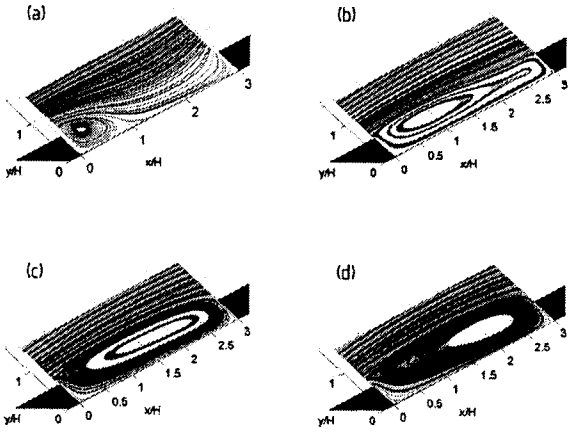

FIG. 3. Streamlines, $D/H=3$, steady calculation

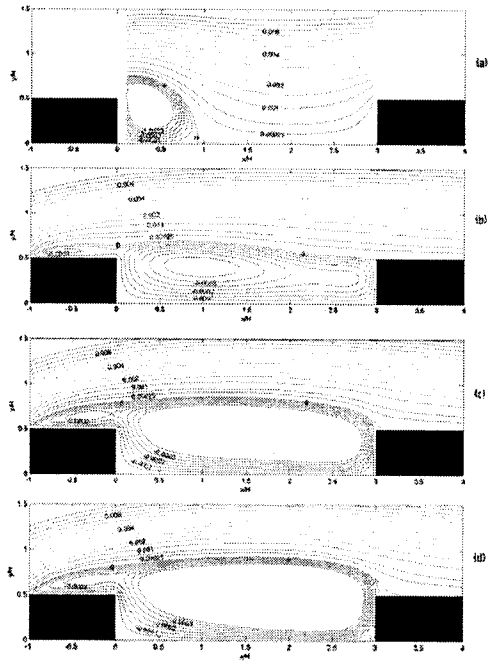

FIG. 4. Contour plots of the stream functions, $D/H=3$, steady calculation

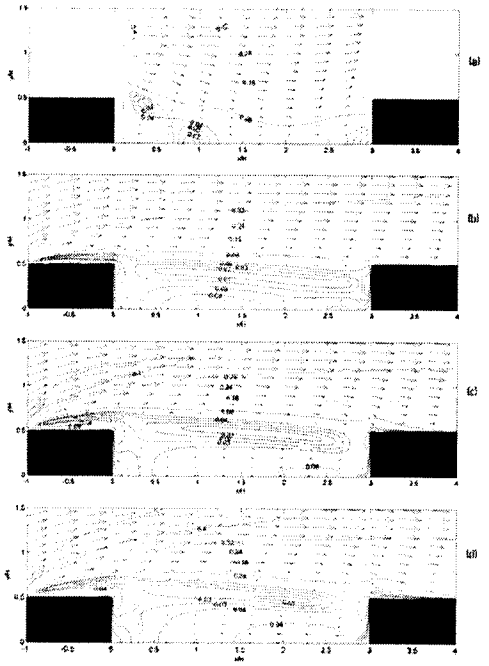

FIG. 5. Contour plots of velocity magnitude and velocity vectors, $D/H = 3$, steady calculation

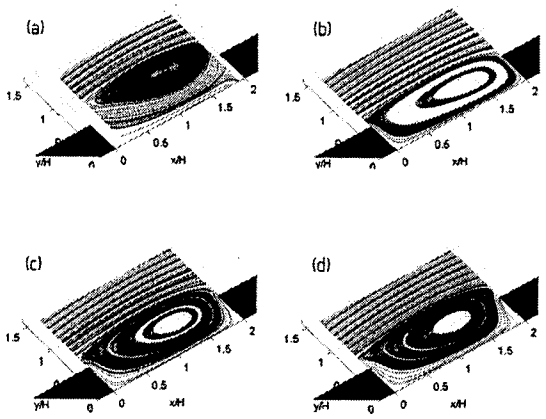

FIG. 6. Streamlines, $D/H = 2$, steady calculation

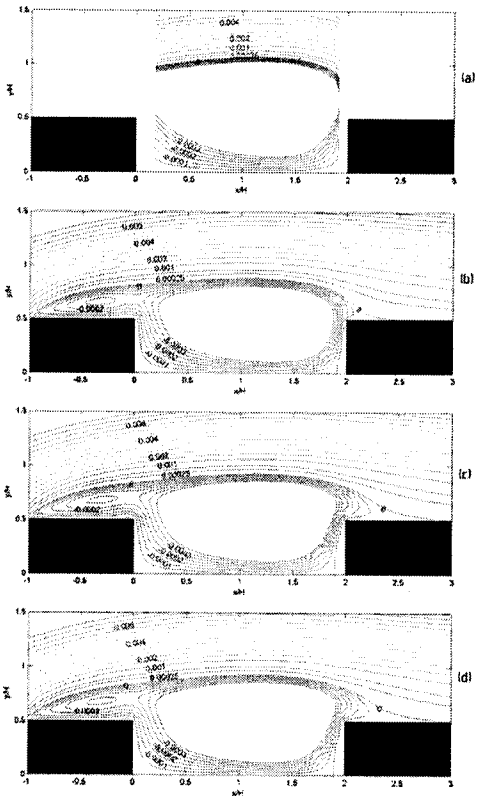

FIG. 7. Contour plots of the stream functions, $D/H = 2$, steady calculation

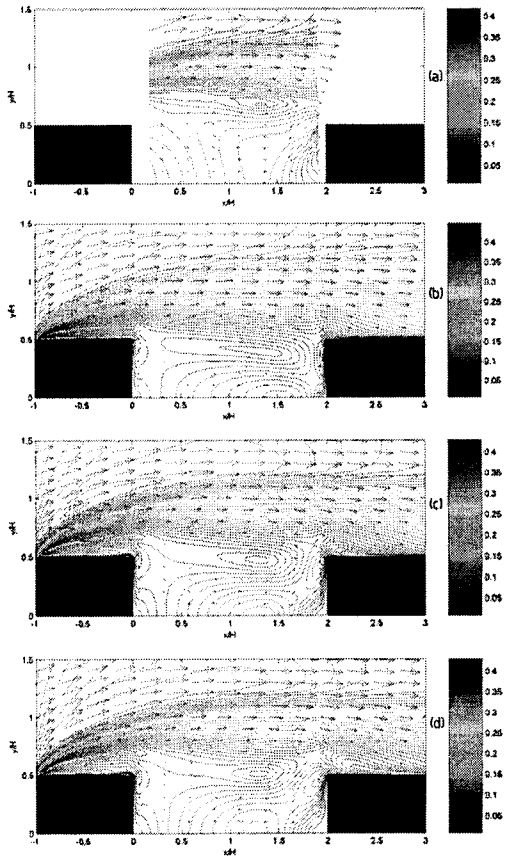

FIG. 8. Contour plots of velocity magnitude and velocity vectors, $D/H = 2$, steady calculation

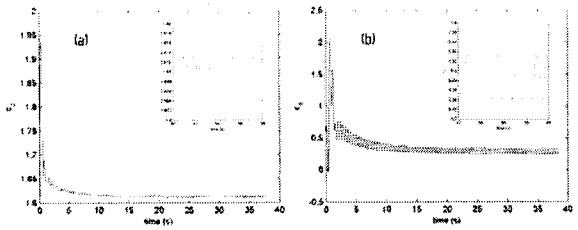

FIG. 9. Drag coefficient c_d over time, $D/H = 3$ (unsteady calculation); (a) upstream cylinder, (b) downstream cylinder

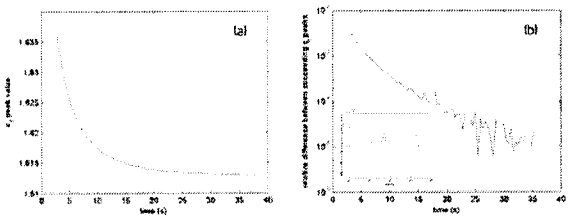

FIG. 10. Convergence of the drag coefficient peaks (upstream cylinder), $D/H = 3$ (unsteady calculation); (a) c_d peaks over time, (b) relative difference $\frac{c_{d,peak,i} - c_{d,peak,i-1}}{c_{d,peak,1}}$

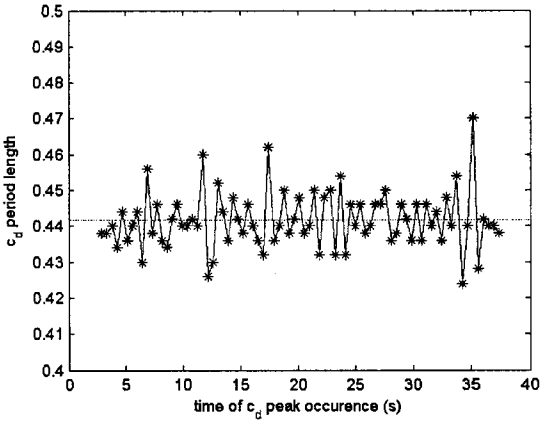

FIG. 11. Length of c_d cycles over time, $D/H = 3$ (unsteady calculation)

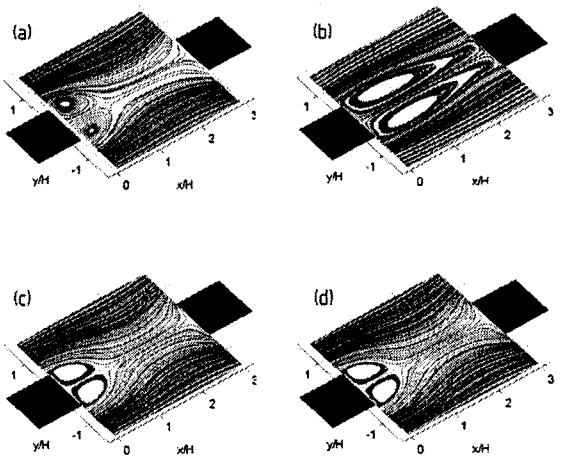

FIG. 12. Streamlines, $D/H = 3$, unsteady calculation

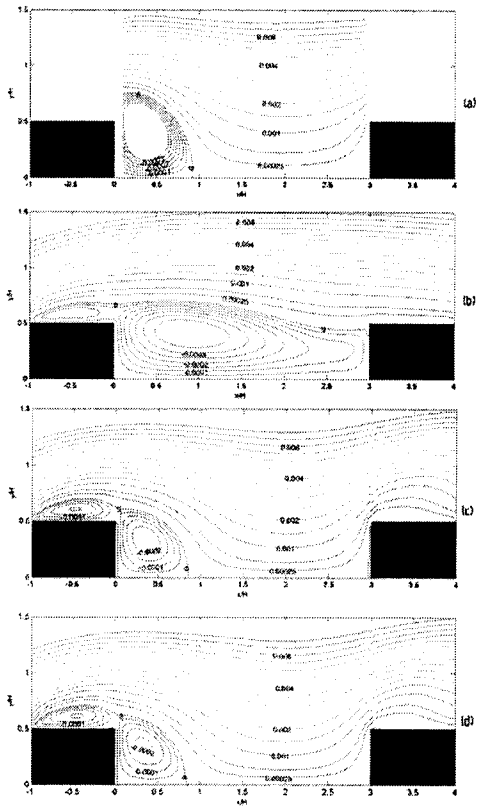

FIG. 13. Contour plots of the stream functions, $D/H=3$, unsteady calculation

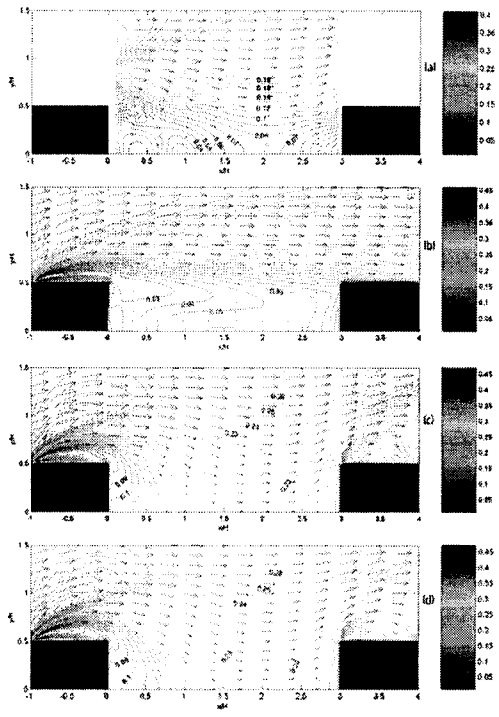

FIG. 14. Contour plots of velocity magnitude and velocity vectors, $D/H=3$, unsteady calculation

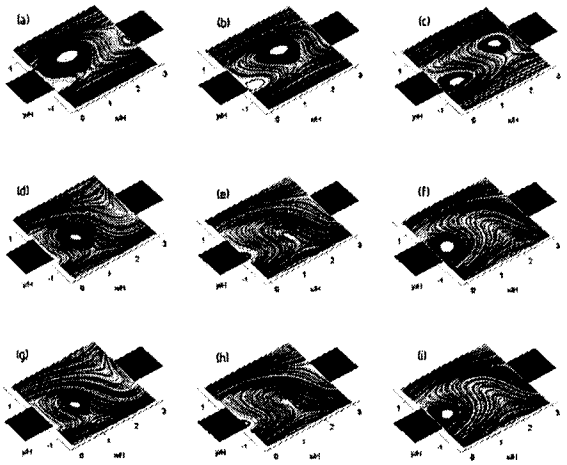

FIG. 15. Streamline plots at different solution times, $D/H=3$; (a)-(c) standard $k-\varepsilon$ model (unsteady, $0.626t_{s,St}$, $0.776t_{s,St}$, $0.926t_{s,St}$), (d)-(f) RNG $k-\varepsilon$ model (unsteady, $0.775t_{s,RN}$, $0.925t_{s,RN}$, $0.075t_{s,RN}$), (g)-(i) realizable $k-\varepsilon$ model (unsteady, $0.675t_{s,\mathrm{Re}}$, $0.826t_{s,\mathrm{Re}}$, $0.976t_{s,\mathrm{Re}}$)

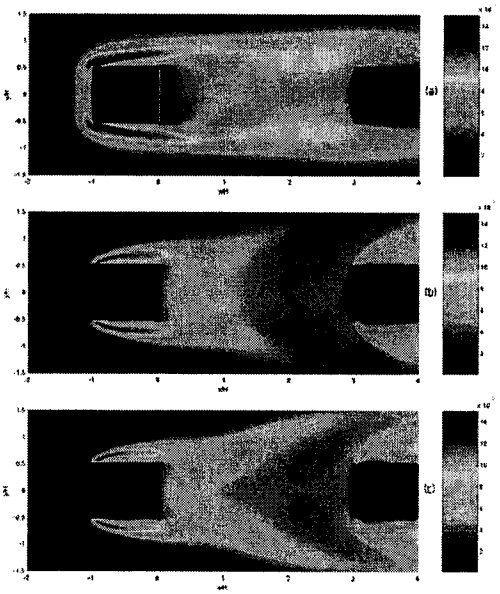

FIG. 16. Ensemble-averaged turbulent kinetic energy k, $D/H=3$; (a) standard $k-\varepsilon$ model (unsteady), (b) RNG $k-\varepsilon$ model (unsteady), (c) realizable $k-\varepsilon$ model (unsteady)

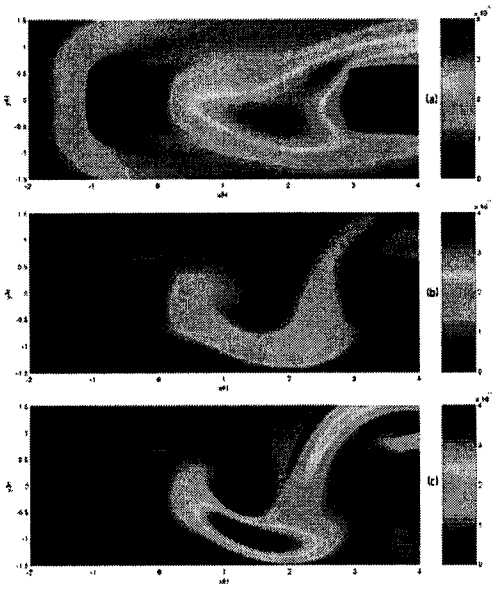

FIG. 17. Eddy viscosity υ_T, $D/H=3$; (a) standard $k-\varepsilon$ model (unsteady, $0.626t_{s,St}$), (b) RNG $k-\varepsilon$ model (unsteady, $0.775t_{s,RN}$), (c) realizable $k-\varepsilon$ model (unsteady, $0.675t_{s,\mathrm{Re}}$)

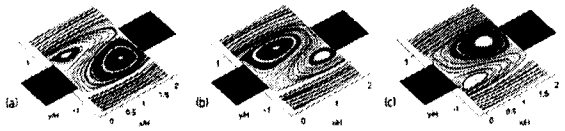

FIG. 18. Streamline plots a different solution times, $D/H=2$; (a)-(c) RNG $k-\varepsilon$ model (unsteady, $0.17t_{s,RN2}$, $0.42t_{s,RN2}$, $0.67t_{s,RN2}$)

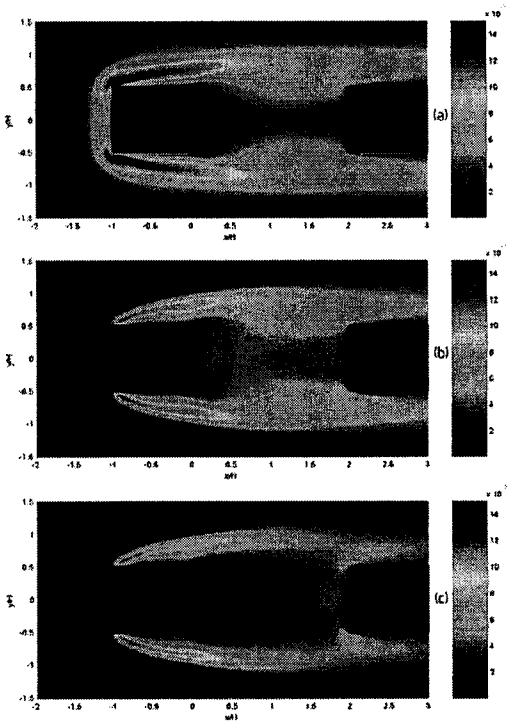

FIG. 19. Ensemble-averaged turbulent kinetic energy k, $D/H=2$; (a) standard $k-\varepsilon$ model (unsteady), (b) RNG $k-\varepsilon$ model (unsteady), (c) realizable $k-\varepsilon$ model (unsteady)

	c_d upstream	c_d downstream	Strouhal number
Experiment	-	-	0.121
Sakamoto et al.	2.28	0.95	-
Standard $k-\varepsilon$	1.61	0.29	0.114
RNG $k-\varepsilon$	1.84	3.51	0.131
Realizable $k-\varepsilon$	1.88	2.30	0.135

TAB 1. Comparison of drag coefficients and *St*, $D/H=3$

	c_d upstream	c_d downstream
Sakamoto et al.	1.75	-0.60
Standard $k-\varepsilon$	1.60	-0.17
RNG $k-\varepsilon$	1.67	-0.30
Realizable $k-\varepsilon$	1.69	-0.39

TAB 2. Comparison of drag coefficients, $D/H=2$